crystals

MDPI

Article

Synthesis, Crystal Structures and Magnetic Properties of Trinuclear {Ni_2Ln} (Ln^{III} = Dy, Ho) and {Ni_2Y} Complexes with Schiff Base Ligands

Despina Dermitzaki [1], Angeliki Panagiotopoulou [2], Michael Pissas [1], Yiannis Sanakis [1], Vassilis Psycharis [1,*] and Catherine P. Raptopoulou [1,*]

[1] Institute of Nanoscience and Nanotechnology, NCSR "Demokritos", Aghia Paraskevi, 15310 Athens, Greece; d.dermitzaki@inn.demokritos.gr (D.D.); m.pissas@inn.demokritos.gr (M.P.); i.sanakis@inn.demokritos.gr (Y.S.)

[2] Institute of Biosciences and Applications, NCSR "Demokritos", Aghia Paraskevi, 15310 Athens, Greece; apanagio@bio.demokritos.gr

* Correspondence: v.psycharis@inn.demokritos.gr (V.P.); c.raptopoulou@inn.demokritos.gr (C.P.R.)

Abstract: The reaction of the Schiff base ligand o-OH-C_6H_4-CH=N-$C(CH_2OH)_3$, H_4L, with $Ni(O_2CMe)_2 \cdot 4H_2O$ and lanthanide nitrate salts in a 4:2:1 ratio lead to the formation of the trinuclear complexes $[Ni_2Ln(H_3L)_4(O_2CMe)_2](NO_3)$ (Ln = Dy (**1**), Ho (**2**), and Y (**3**)) which crystallize in the non-centrosymmetric space group *P*na2_1. The complex cation consists of the three metal ions in an almost linear arrangement. The {Ni_2Ln} moieties are bridged through two deprotonated $O_{phenolato}$ groups from two different ligands. Each terminal Ni^{II} ion is bound to two ligands through their $O_{phenolato}$, the N_{imino} atoms and one of the protonated O_{alkoxo} groups in a distorted octahedral. The central lanthanide ion is coordinated to four $O_{phenolato}$ oxygen from the four ligands, and four $O_{carboxylato}$ atoms from two acetates which are bound in the bidentate chelate mode, and the coordination polyhedron is biaugmented trigonal prism, which probably results in a non-centrosymmetric arrangement of the complexes in the lattice. The magnetic properties of **1**–**3** were studied and showed that **1** exhibits field induced slow magnetic relaxation.

Keywords: heterotrinuclear complexes; nickel; lanthanides; Schiff base; magnetic properties; crystal structure

Citation: Dermitzaki, D.; Panagiotopoulou, A.; Pissas, M.; Sanakis, Y.; Psycharis, V.; Raptopoulou, C.P. Synthesis, Crystal Structures and Magnetic Properties of Trinuclear {Ni_2Ln} (Ln^{III} = Dy, Ho) and {Ni_2Y} Complexes with Schiff Base Ligands. *Crystals* **2022**, *12*, 95. https://doi.org/10.3390/cryst12010095

Academic Editor: Ana M. Garcia-Deibe

Received: 16 December 2021
Accepted: 8 January 2022
Published: 11 January 2022

1. Introduction

The study of multifunctional materials, with new or combined properties, is a very active area in material science, as new materials are expected to have a big impact on new technologies that possibly could be the driving force for economic growth in the near future [1]. In multifunctional materials, two or more physical properties are combined on the same entity or different entities or subunits of the material, and one could be used to monitor the other by external or internal stimuli [2]. In this respect, molecular materials could play a vital role, as their diverse properties/functions can be tailored by chemical design and synthesis, following a bottom-up approach and by using principles of coordination chemistry, i.e., the appropriate metal or metals coordinated with the proper ligands. The field of multifunctional Single Molecule Magnets (SMMs) is growing rapidly as it is proved by the pioneering works that have resulted on the synthesis of complexes that combine the SMM behavior with conductivity [3], ferroelectricity [4], dielectricity [5], luminescence [6] and chirality [5,7]. Many examples of pure transition metal or lanthanide complexes exist, which exhibit, in addition to the SMM properties, an extra property that classify them as multifunctional materials [3,6,8].

After the observation of the ferromagnetic coupling of Cu^{II} with Gd^{III} in two mixed metal complexes, a route was opened and the 3d/4f mixed metal complexes prepared

afterwards have provided excellent examples with SMM properties [9–11]. Mixed 3d/4f metal complexes present a strong magnetocaloric effect [12] or luminescence properties [13]. In addition, enantiopure mixed metal complexes combine the SMM properties with ferroelectricity [14] or, in the case of the Zn/Dy [15] complex, it presents additionally luminescence properties. The last examples indicate that the introduction of chirality in a magnetic system is a probable route to multifunctionality as in the case of transition metal complexes [2]. As the trinuclear mixed 3d/4f metal systems have provided interesting examples with SMM properties [16,17], recently we have focused our research on the Ni^{II}-Ln^{III}-Ni^{II} system [18,19]. In these series of compounds, there are examples which present also SMM properties [20–23] or the magnetocaloric effect [24]. The crystal structure study of the series of $[Ni_2Ln(H_3L)_4(O_2CMe)_2](NO_3)$ (Ln = Sm, Eu, Gd, Tb)] complexes [19] indicate that all the compounds are isomorphous and they crystallize in the centrosymmetric orthorhombic space group *P*nnn and the study of their magnetic properties study indicate that the Ln^{III} = Gd complex presents magnetocaloric behavior. Based on the literature survey for the linear Ni^{II}-Ln^{III}-Ni^{II} system presented in [18], there are cases where the complexes are chiral and, as they crystallize in centrosymmetric space groups, both enantiomers exist in the structure [25,26].

In this study we present the synthesis, crystallographic characterization and magnetic properties of three complexes $[Ni_2Ln(H_3L)_4(O_2CMe)_2](NO_3)$ (Ln = Dy (**1**), Ho (**2**), and Y (**3**)) which were synthesized following the same synthetic paths as previously described [19], but all three complexes crystallize in the non-centrosymmetric *P*na2_1 space group which belongs to the mm^2 point group (following the standard notation). This point group, along with the axial and the m point groups, belong to the seven point groups which lie in the section where interesting electrical or optical properties could coexist. Thus, either the size of lanthanide(III) ion or intermolecular interactions probably result in the crystallization of these complexes to a space group which belongs to the appropriate point group, for the studied material to have multifunctional properties. The crystal structure characteristics of the three complexes are also discussed within this context.

2. Materials and Methods

All manipulations were performed under aerobic conditions using materials as received (Aldrich Co., London, UK). All chemicals and solvents were of reagent grade. The ligand OH-C_6H_4-CH=NC$(CH_2OH)_3$, H_4L was synthesized as described previously [27]. Elemental analysis for carbon, hydrogen, and nitrogen was performed on a PerkinElmer (Waltham, MA, USA) 2400/*II* automatic analyzer. Infrared spectra were recorded as KBr pellets in the range 4000–400 cm^{-1} on a Bruker Equinox 55/S FT-IR spectrophotometer. Variable-temperature magnetic susceptibility measurements were carried out on polycrystalline samples of **1**, **2** and **3** by using a Quantum Design PPMS 9T and a SQUID magnetometer (Quantum Design MPMS 5.5). Diamagnetic corrections were estimated from Pascal's constants.

2.1. Compound Preparations

2.1.1 $[Ni_2Dy(H_3L)_4(O_2CMe)_2](NO_3)\cdot 3MeOH\cdot H_2O$ (**1**·3MeOH·H_2O). Solid $Dy(NO_3)_3\cdot 5H_2O$ (0.25 mmol, 0.1096 g) was added under stirring to a yellow solution of H_4L (1.00 mmol, 0.2252 g) in MeOH (20 mL). The solution was refluxed for three hours until solid $Ni(O_2CMe)_2\cdot 4H_2O$ (0.50 mmol, 0.1244 g) was added and continue refluxing for two more hours. The final green solution was layered with a mixture of Et_2O/n-hexane (1:1 *v*/*v*) to afford light green X-ray quality single crystals after approximately two weeks. The material was filtered off and dried in vacuo. Yield: 0.058 g, ~17% based on Dy^{III}. $C_{48}H_{62}N_5O_{23}Ni_2Dy$ (**1**) (fw = 1356.96) requires C, 42.49; H, 4.61; N, 5.16%. Found: C, 42.40; H, 4.59; N, 5.14%. FT-IR (KBr pellets, cm^{-1}): 3416 (br), 2980 (w), 2935 (w), 2886 (w), 1600 (vs), 1556 (vs), 1524 (m), 1475 (vs), 1446 (vs), 1408 (m), 1384 (vs), 1349 (m), 1320 (s), 1283 (vs), 1253 (m), 1200 (s), 1166 (m), 1149 (s), 1140 (s), 1053 (vs), 1040 (vs), 977 (m), 946 (s), 922 (m), 891 (s), 864 (m), 816 (s), 775 (m), 761 (vs), 744 (s), 680 (s), 636 (s), 580 (m), 524 (m), 457 (s).

2.1.2 $[Ni_2Ho(H_3L)_4(O_2CMe)_2](NO_3)\cdot 2EtOH\cdot 3H_2O$ (**2**·2EtOH·3H_2O). Solid $Ho(NO_3)_3\cdot 5H_2O$ (0.25 mmol, 0.1103 g) was added under stirring to a yellow solution of H_4L (1.00 mmol, 0.2252 g) in EtOH (20 mL). The solution was refluxed for three hours until solid $Ni(O_2CMe)_2\cdot 4H_2O$ (0.50 mmol, 0.1244 g) was added and refluxing was then continued for two more hours. The final green solution was layered with a mixture of Et_2O/n-hexane (1:1 v/v) to afford light green X-ray quality single crystals after approximately two weeks. The material was filtered off and dried in vacuo. Yield: 0.071 g, ~21% based on Ho^{III}. $C_{48}H_{62}N_5O_{23}Ni_2Ho$ (**2**) (fw = 1359.39) requires C, 42.41; H, 4.60; N, 5.15%. Found: C, 42.32; H, 4.58; N, 5.13%. FT-IR (KBr pellets, cm^{-1}): 3443 (br), 2919 (m), 2846 (m), 1602 (s), 1556 (s), 1473 (s), 1444 (s), 1384 (vs), 1353 (sh), 1320 (w), 1284 (s), 1251 (m), 1199 (m), 1150 (m), 1124 (m), 1048 (s), 942 (m), 890 (m), 855 (w), 810 (m), 768 (m), 741 (w), 730 (w), 717 (w), 684 (w), 670 (w), 632 (w), 612 (w), 586 (w), 544 (w), 481 (w), 453 (w).

2.1.3 $[Ni_2Y(H_3L)_4(O_2CMe)_2](NO_3)\cdot 3MeOH\cdot H_2O$ (**3**·3MeOH·H_2O). Solid $Y(NO_3)_3\cdot 5H_2O$ (0.25 mmol, 0.0912 g) was added under stirring to a yellow solution of H_4L (0.50 mmol, 0.1126 g) and $NaO_2CMe\cdot 3H_2O$ (0.50 mmol, 0.0680 g) in MeOH (20 mL). The solution was refluxed for three hours until solid $Ni(O_2CMe)_2\cdot 4H_2O$ (0.25 mmol, 0.0622 g) was added and refluxing was then continued for two more hours. The final green solution was layered with a mixture of Et_2O/n-hexane (1:1 v/v) to afford light green X-ray quality single crystals after approximately two weeks. The material was filtered off and dried in vacuo. Yield: 0.048 g, ~18% based on Y^{III}. $C_{48}H_{62}N_5O_{23}Ni_2Y$ (**3**) (fw = 1283.37) requires C, 44.92; H, 4.87; N, 5.46%. Found: C, 44.83; H, 4.85; N, 5.44%. FT-IR (KBr pellets, cm^{-1}): 3443 (br), 2940 (w), 2855 (w), 1599 (vs), 1556 (vs), 1474 (vs), 1446 (s), 1384 (vs), 1341 (m), 1317 (m), 1285 (vs), 1253 (m), 1201 (s), 1150 (s), 1125 (m), 1045 (vs), 943 (m), 889 (s), 859 (m), 809 (s), 774 (vs), 740 (m), 687 (m), 634 (m), 611 (m), 583 (m), 546 (w), 523 (w), 478 (w), 453 (m).

2.2. Single Crystal X-ray Crystallography

Crystals of **1**·3MeOH·H_2O (0.15 × 0.37 × 0.52 mm), **2**·2EtOH·3H_2O (0.06 × 0.09 × 0.26 mm) and **3**·3MeOH·H_2O (0.09 × 0.14 × 0.29 mm) were taken from the mother liquor and immediately cooled to −113 °C. Diffraction measurements were made on a Rigaku R-AXIS SPIDER Image Plate diffractometer using graphite monochromated Cu Kα radiation. Data collection (ω-scans) and processing (cell refinement, data reduction and empirical/numerical absorption correction) were performed using the CrystalClear program package [28]. The structures were solved by direct methods using SHELXS v.2013/1 and refined by full-matrix least-squares techniques on F^2 with SHELXL ver2014/6 [29,30]. The absolute structure of **1**–**3**, which crystallizes in the non-centrosymmetric space group, was determined by refined as 2-component inversion twin using TWIN and BASF instructions, with Flack parameter x, equals to 0.016(4), 0.554(8) and 0.12(2), respectively. Important crystallographic and refinement data are listed in Table 1. Further experimental crystallographic details for **1**·3MeOH·H_2O: $2\theta_{max}$ = 130°; reflections collected/unique/used, 75,433/10,191 [R_{int} = 0.0672]/10,191; 793 parameters refined; $(\Delta/\sigma)_{max}$ = 0.001; $(\Delta\rho)_{max}/(\Delta\rho)_{min}$ = 1.298/−1.191 e/Å^3; $R1/wR2$ (for all data), 0.0474/0.1269. Further experimental crystallographic details for **2**·2EtOH·3H_2O: $2\theta_{max}$ = 130°; reflections collected/unique/used, 65,395/9926 [R_{int} = 0.0267]/9926; 812 parameters refined; $(\Delta/\sigma)_{max}$ = 0.003; $(\Delta\rho)_{max}/(\Delta\rho)_{min}$ = 0.753/−0.426 e/Å^3; $R1/wR2$ (for all data), 0.0337/0.0808. Further experimental crystallographic details for **3**·3MeOH·H_2O: $2\theta_{max}$ = 130°; reflections collected/unique/used, 56,144/10,094 [R_{int} = 0.0430]/10,094; 736 parameters refined; $(\Delta/\sigma)_{max}$ = 0.003; $(\Delta\rho)_{max}/(\Delta\rho)_{min}$ = 1.626/−1.195 e/Å^3; $R1/wR2$ (for all data), 0.0659/0.1731. Hydrogen atoms were introduced at calculated positions as riding on bonded atoms. All non-hydrogen atoms were refined anisotropically. Plots of the structure were drawn using the Diamond 3 program package [31].

Table 1. Crystallographic data (see Appendix A) for **1**·3MeOH·H_2O, **2**·2EtOH·3H_2O and **3**·3MeOH·H_2O.

	1·3MeOH·H_2O	**2·2EtOH·3H_2O**	**3·3MeOH·H_2O**
Formula	$C_{48}H_{62}DyN_5Ni_2O_{23}·3(CH_4O)·(H_2O)$	$C_{48}H_{62}HoN_5Ni_2O_{23}·2(C_2H_6O)·3(H_2O)$	$C_{48}H_{62}N_5Ni_2O_{23}Y·3(CH_4O)·(H_2O)$
F.w.	1471.08	1505.56	1397.49
Space group	*P*na2$_1$	*P*na2$_1$	*P*na2$_1$
a (Å)	26.4216(5)	26.4211(5)	26.4052(5)
b (Å)	10.1714(2)	10.1651(2)	10.1074(2)
c (Å)	22.9439(4)	22.8249(4)	22.8177(4)
V (Å^3)	6166.1(2)	6130.2(2)	6089.8(2)
Z	4	4	4
T (°C)	−113	−113	−113
Radiation	Cu Kα 1.54178	Cu Kα 1.54178	Cu Kα 1.54178
ρ_{calcd}, g cm^{-3}	1.585	1.631	1.524
μ, mm^{-1}	7.845	3.806	2.728
Reflections with $I > 2\sigma(I)$	9688	9548	9392
R_1 [a]	0.0457	0.0319	0.0611
wR_2 [a]	0.1251	0.0793	0.1651

[a] $w = 1/[\sigma^2(F_o^2) + (\alpha P)^2 + bP]$ and $P = (\max F_o^2,0) + 2F_c^2)/3$, $a = 0.0786$, $b = 4.6125$ (**1**); $a = 0.0428$, $b = 6.5995$ (**2**); $a = 0.1023$, $b = 14.2398$ (**3**), $R_1 = \Sigma(|F_o| - |F_c|)/\Sigma(|F_o|)$ and $wR_2 = \{\Sigma[w(F_o^2 - F_c^2)^2]/\Sigma[w(F_o^2)^2]\}^{1/2}$.

3. Results

3.1. Synthesis and IR Spectroscopic Characterization

Previously we have reported the trinuclear complexes $[Ni_2Ln(H_3L)_4(O_2CMe)_2](NO_3)$ (Ln^{III} = Sm, Eu, Gd, Tb), which were isolated by the 4:2:1 $H_4L/Ni(O_2CMe)_2·4H_2O/Ln(NO_3)_3·6H_2O$ molar ratio reaction in EtOH [19]. The crystal structure of the {Ni_2Tb} complex revealed that the Tb^{III} ion is linked to each of the Ni^{II} ions via two $O_{phenolato}$ atoms of the $(H_3L)^-$ ligands and contains a strictly linear Ni^{II}-Tb^{III}-Ni^{II} moiety. An extensive network of hydrogen bonds, due to the presence of protonated alkoxide groups of the ligands, gave rise to the lattice structure of the complex which consists of two 3D interpenetrating supramolecular diamond-like lattices. The magnetic study of the {Ni_2Gd} complex revealed ferromagnetic coupling between the metal ions leading to ground state of total spin $S = 11/2$, whereas antiferromagnetic coupling was found for the remaining three complexes. To study the influence of the lanthanide to the nature of the magnetic exchange between the metal ions we have performed analogous reactions with Ln^{III} = Dy, Ho and the diamagnetic Y^{III} ion.

The trinuclear complexes **1** and **2** were prepared by the stoichiometric reaction of two equivalents of $Ni(O_2CMe)_2·4H_2O$ with one equivalent of $Ln(NO_3)_3·5H_2O$ (**1**: Dy^{III}; **2**: Ho^{III}) and four equivalents of H_4L in MeOH (**1**) or EtOH (**2**), respectively. The 1:1:2 $Ni(O_2CMe)_2·4H_2O/Y(NO_3)_3·5H_2O/H_4L$ molar ratio reaction in MeOH in the presence of two equivalents of $NaO_2CMe·3H_2O$ afforded the trinuclear complex **3**. Precipitation of single-crystals of **1**–**3** was achieved by layering of the reaction solution with mixture of Et_2O/*n*-hexane. If compounds **1**–**3** are the only products of the reaction, their formation can be described by the following equation:

$$2Ni(O_2CMe)_2 \cdot 4H_2O + Ln(NO_3)_3 \cdot 5H_2O + 4H_4L \xrightarrow{ROH} [Ni_2Ln(H_3L)_4(O_2CMe)_2](NO_3) + 2HNO_3 + 2HO_2CMe + 13H_2O \quad (1)$$

1 − 3

The excess of acetates in the reaction solution which afforded single crystals of **3** did not increased the deprotonation state of the ligand or the identity of the product. Moreover, complex **3** was the only product of the reaction which was isolated under the specific crystallization conditions.

The IR spectra of the three complexes exhibit broad bands at 3416 and 3443 cm^{-1} attributed to the ν(OH) vibrations due to the presence of protonated alkoxide groups of the

ligands. The band at ~1600 cm^{-1} is attributed to the ν(C=N) vibration. The shifting of this band to a lower frequency with respect to that of the free ligand (~1635 cm^{-1}) in the spectra of **1**–**3** suggests coordination of the metal ions through the imino nitrogen. The ν(C-O) stretching frequency of the phenolic oxygen of the ligand is seen at 1395 cm^{-1} and shifts to a lower frequency in the spectra of all complexes, in the range of 1313–1320 cm^{-1}, indicating coordination to the metal ions [32]. The strong bands at ~1555 and ~1444 cm^{-1} are attributed to the $\nu_{as}(CO_2)$ and $\nu_s(CO_2)$ stretching vibrations of the bidentate chelate acetato ligands. The difference $\Delta = \nu_{as}(CO_2) - \nu_s(CO_2)$ is 110–112 cm^{-1} and is in agreement with the low difference values found in rare earth acetates with chelating coordination mode [33–35]. The strong band at 1384 cm^{-1} in the spectra **1**–**3** is attributed to the presence of the $\nu_3(E')$ [ν_d(NO)] mode of the uncoordinated D_{3h} ionic nitrates [36].

3.2. Description of the Structures

Compounds $[Ni_2Ln(H_3L)_4(O_2CMe)_2](NO_3)$ (Ln = Dy^{III} (**1**), Ho^{III} (**2**), Y^{III} (**3**)) are isomorphous and crystallize in the non-centrosymmetric orthorhombic space group $Pna2_1$. The asymmetric unit cell contains one trinuclear cation, one nitrate counteranion and solvate molecules; the latter will not be discussed further. The Ni_2Ln moiety is almost linear with Ni···Ln···Ni angles 174.6 (**1**: Dy^{III}), 173.8 (**2**: Ho^{III}) and 174.5° (**3**: Y^{III}). The interatomic distances Ni···Ln are Dy(1)···Ni(1) = 3.421(1) Å, Dy(1)···Ni(2) = 3.441(1) Å, Ho(1)···Ni(1) = 3.403(1) Å, Ho(1)···Ni(2) = 3.436(1) Å, Y(1)···Ni(1) = 3.405(2) Å, and Y(1)···Ni(2) = 3.433(2) Å. The central Ln^{III} is bridged to each of the terminal Ni^{II} ions through two deprotonated $O_{phenolato}$ atoms from two different ligands (Figure 1a, Table 2). The Ni^{II} ions are coordinated to two ligands through their $O_{phenolato}$, the N_{imino} nitrogen and one of the protonated O_{alkoxo} groups in distorted octahedral geometry. The Ln^{III} ion is coordinated to four $O_{phenolato}$ atoms from the four ligands, and four $O_{carboxylato}$ atoms from two acetates which are bound in the bidentate chelate mode. Continuous Shape Measures by using the program SHAPE [37] show that the best-fit polyhedron around the Ln^{III} ion is the biaugmented trigonal prism, BTPR-8, (Figure 1b) with CShM = 2.89088 (**1**), 2.82693 (**2**) and 2.83263 (**3**).

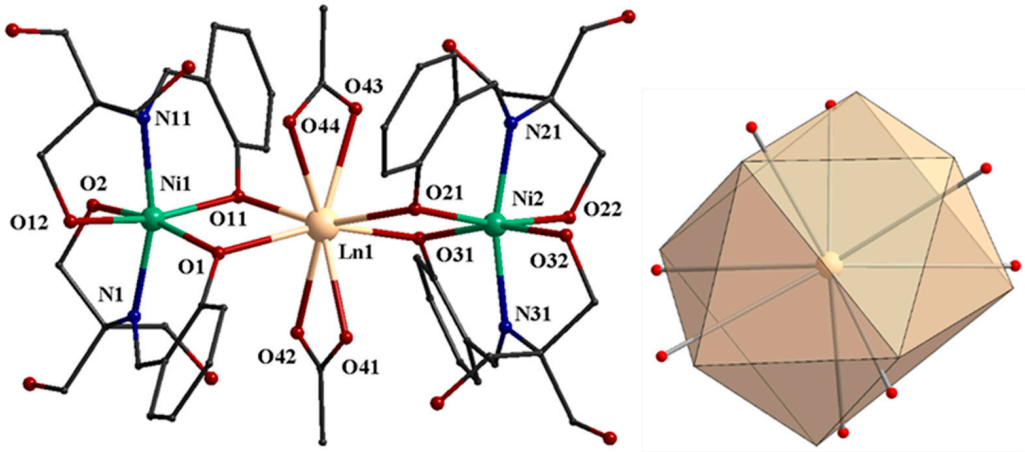

(**a**) (**b**)

Figure 1. (**a**) Partially labeled plot of the cationic part of **1**–**3**; hydrogen atoms are omitted for clarity. Color code: Ni^{II} green; Ln^{III} = Dy(**1**), Ho(**2**), Y(**3**) tan; O, red; N, blue; C, grey. (**b**) The biaugmented trigonal prism around the Ln^{III} ion.

Table 2. Selected bond distances (Å) in **1**·3MeOH·H_2O, **2**·2EtOH·3H_2O and **3**·3MeOH·H_2O.

	1·3MeOH·H_2O	**2**·2EtOH·3H_2O	**3**·3MeOH·H_2O
Ln(1)-O(11)	2.312(4)	2.293(3)	2.298(6)
Ln(1)-O(31)	2.306(5)	2.300(4)	2.297(6)
Ln(1)-O(21)	2.354(5)	2.347(3)	2.341(6)
Ln(1)-O(1)	2.355(5)	2.330(4)	2.341(6)
Ln(1)-O(41)	2.429(5)	2.421(4)	2.419(6)
Ln(1)-O(44)	2.435(5)	2.416(3)	2.425(6)
Ln(1)-O(43)	2.454(5)	2.446(4)	2.443(6)
Ln(1)-O(42)	2.468(5)	2.443(4)	2.446(6)
Ni(1)-N(1)	2.033(6)	2.023(4)	2.038(8)
Ni(1)-N(11)	2.048(7)	2.044(4)	2.041(8)
Ni(1)-O(11)	2.056(5)	2.049(4)	2.050(7)
Ni(1)-O(1)	2.053(5)	2.053(4)	2.045(6)
Ni(1)-O(2)	2.079(6)	2.075(4)	2.076(7)
Ni(1)-O(12)	2.085(6)	2.090(4)	2.116(7)
Ni(2)-N(31)	2.037(7)	2.050(4)	2.038(8)
Ni(2)-N(21)	2.035(6)	2.037(4)	2.024(8)
Ni(2)-O(21)	2.057(5)	2.053(4)	2.055(6)
Ni(2)-O(31)	2.062(5)	2.063(4)	2.062(7)
Ni(2)-O(32)	2.082(5)	2.076(4)	2.069(7)
Ni(2)-O(22)	2.091(6)	2.091(4)	2.086(8)

The arrangement of ligands around the metal center's creates a Δ-Δ-Δ configuration for the complex at (x, y, z) position (left image at Figure 2) and a Λ-Λ-Λ one for its mirror image ($0.5 - x$, $-0.5 + y$, $0.5 + z$ position, right image, Figure 2). The complexes studied in the present study are isostructural with the complex of {Ni_2Tb} studied previously [19], as is revealed in Figure S1. Although, the CShM parameter differs slightly for the two polyhedrons around Tb^{III} in {Ni_2Tb} and Dy^{III} in **1** (Table S1, Figure S2), the movement of O(1) and O(21) (Figure 1a) atoms toward the center of the trigonal prism faces, transforms a square antiprism polyhedron ({Ni_2Tb} case) to a biaugmented trigonal prism one (Dy, Ho and Y in the present study).

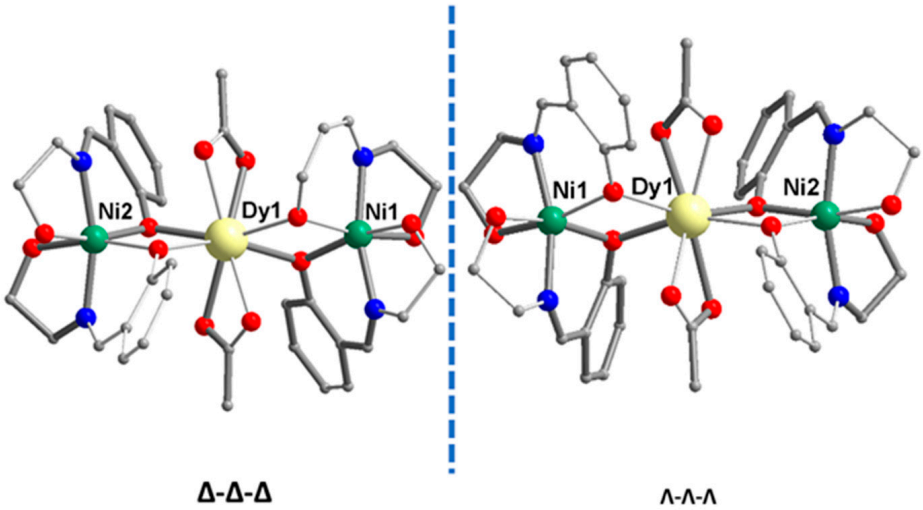

Figure 2. Enantiomeric mirror images in the structure of the complexes **1**, **2** and **3**.

In all three structures, different types of hydrogen bonds are observed, i.e., intramolecular ones (Table 3) which stabilize the observed configuration of the complexes, as well as intermolecular hydrogen bonds which built the supramolecular structure. Each trinuclear cation acts as 6-connected node and is linked to six neighboring clusters through ten hydrogen bonds developed between the protonated pendant alkoxide groups of $(H_3L)^-$ and form an overall 3D supramolecular network (Figure 3). Figure S3 compares the packing observed

in the structure of {Ni_2Tb} [19] and **1** where we observe important differences. Although in both structures the hydrogen bonds are among protonated pendant alkoxide groups of $(H_3L)^-$ ligand, in the case of the {Ni_2Tb} complex, the axes of the trinuclear complexes are parallel to each other along all crystallographic directions. In the case of **1**, they remain parallel to each other only along the *c* axis, whereas along the other directions the axes are inclined as compared to the central one (Figure S3). Probably the slight differences in the type of polyhedron around the Ln^{III} atom have caused small differences in the arrangement of protonated pendant alkoxide groups which play an anchor role, and thus promote a different arrangement of neighboring complexes, which results in different packing and, finally, in a different space group. In all studied structures from this family of compounds, solvents are trapped in the lattice, which interact through intermolecular bonds with the complexes (Table 3) and thus, in addition to the other physical properties, these compounds could be useful as host lattices of different solvents.

Table 3. Hydrogen bonds in **1**·3MeOH·H_2O, **2**·2EtOH·3H_2O and **3**·3MeOH·H_2O.

Interaction	D···A (Å)	H···A (Å)	D-H···A (°)	Symmetry Operation
		1·3MeOH·H_2O		
		Intramolecular		
O(4)-H(4O)···O(42)	2.695	1.879	163.5	x, y, z
O(13)-H(13O)···O(44)	2.672	1.837	172.4	x, y, z
O(22)-H(22O)···O(52)	2.947	2.154	157.2	x, y, z
O(23)-H(23O)···O(43)	2.666	1.921	147.2	x, y, z
O(34)-H(34O)···O(41)	2.670	1891	153.1	x, y, z
		Intermolecular among complexes		
O(3)-H(3O)···O(33)	2.703	1.911	156.7	$0.5 - x, -0.5 + y, -0.5 + z$
O(14)-H(14O)···O(34)	2.672	1.836	173.6	$0.5 + x, 2.5 - y, z$
O(24)···O(14)	2.919			$1 - x, 2 - y, 0.5 + z$
O(33)-H(33O)···O(13)	2.678	1.715	161.0	$-0.5 + x, 2.5 - y, z$
		Intermolecular among complexes and lattice solvents		
O(12)-H(12O)···O(1 m)	2.731	2.242	117.2	$0.5 - x, 0.5 + y, -0.5 + z$
O(2)-H(2O)···O(1 w)	2.618	1.858	149.7	$0.5 - x, 1.5 - y, z$
O(32)-H(32O)···O(2 m)	2.627	1.797	169.5	$x, 1 + y, z$
		2·2EtOH·3H_2O		
		Intramolecular		
O(4)-H(4O)···O(42)	2.712	1.882	169.6	x, y, z
O(13)-H(13O)···O(44)	2.682	1.849	170.9	x, y, z
O(22)-H(22O)···O(53)	2.855	2.061	157.5	x, y, z
O(23)-H(23O)···O(43)	2.685	1.850	172.0	x, y, z
O(34)-H(34O)···O(41)	2.669	1.837	170.4	x, y, z
		Intermolecular among complexes		
O(3)-H(3O)···O(33)	2.726	1.895	169.6	$0.5 - x, -0.5 + y, -0.5 + z$
O(14)-H(14O)···O(34)	2.661	1.823	174.7	$0.5 + x, 2.5 - y, z$
O(24)-H(24O)···O(14)	2.805	1.979	167.6	$1 - x, 2 - -y, 0.5 + z$
O(33)-H(33O)···O(13)	2.679	1.841	176.0	$-0.5 + x, 2.5 - y, z$

Table 3. *Cont.*

Interaction	D···A (Å)	H···A (Å)	D-H···A (°)	Symmetry Operation
Intermolecular among complexes and lattice solvents				
O(12)-H(12O)···O(2 e)	2.649	1.835	162.6	$0.5 - x, 0.5 + y, -0.5 + z$
O(2)-H(2O)···O(1 e)	2.623	1.812	161.7	$0.5 + x, 1.5 - y, z$
O(32)-H(32O)···O(1 w)	2.657	1.833	166.3	$x, 1 + y, z$
O(1e)-H(1Oe)···O(2 w)	2.651	1.843	160.9	$0.5 - x, 0.5 + y, -0.5 + z$
O(2e)-H(2Oe)···O(23)	2.774	1.951	166.2	$-0.5 + x, 1.5 - y, z$
3·3MeOH·H_2O				
Intramolecular				
O(4)-H(4O)···O(42)	2.685	1.854	170.1	x, y, z
O(13)-H(13O)···O(44)	2.672	1.865	160.8	x, y, z
O(22)-H(22O)···O(52)	2.994	2.199	157.8	x, y, z
O(23)-H(23O)···O(43)	2.686	1.894	156.5	x, y, z
O(34)-H(34O)···O(41)	2.657	1.872	154.8	x, y, z
Intermolecular among complexes				
O(3)-H(3O)···O(33)	2.710	1.871	177.1	$0.5 - x, -0.5 + y, -0.5 + z$
O(14)···O(34)	2.645			$0.5 + x, 2.5 - y, z$
O(24)···O(14)	2.927			$1 - x, 2 - y, 0.5 + z$
O(33)-H(33O)···O(13)	2.671	1.926	147.2	$-0.5 + x, 2.5 - y, z$
Intermolecular among complexes and lattice solvents				
O(12)-H(12O)···O(2)	3.060	2.593	116.4	x, y, z
O(2)-H(2O)···O(1 w)	2.568	1.771	157.6	$0.5 + x, 1.5 - y, z$
O(32)-H(32O)···O(2 m)	2.690	1.865	167.3	$x, 1 + y, z$

3.3. Magnetic Measurements

The temperature dependence of the magnetic susceptibility in the form of $\chi_M T$ vs. T under a magnetic field of 1 kOe is shown in Figure 4. The $\chi_M T$ product of complex **1** at 300 K is 16.87 cm^3Kmol^{-1} which compares with the theoretical value of 16.15 cm^3Kmol^{-1} for two non-interacting Ni^{II} ($S = 1$, $g = 2.0$) and one Dy^{III} ($S = 5/2$, $J = 15/2$, $g = 4/3$) ions. Upon cooling, the $\chi_M T$ product decreases slowly to the value of 14.54 cm^3Kmol^{-1} at 10 K and then drops more rapidly to the value of 12.36 cm^3Kmol^{-1} at 2 K (Figure 4). The slight decrease in the value of the $\chi_M T$ product down to 10 K is probably due to the thermal depopulation of the dysprosium excited states. The field dependence of the magnetization at 2 K reaches a value of 9.48 μ_B at 80 kOe without reaching saturation (Figure 4, inset).

The magnetic relaxation properties of **1** were monitored by ac magnetic susceptibility measurements. In the absence of an external magnetic field, no out-of-phase signals are observed down to 2 K when applying frequencies of up to 10 kHz. Slow relaxation is induced in the presence of small magnetic fields. Good conditions for monitoring the relaxation properties were obtained for H_{DC} = 1.0 kOe. The plots of the temperature dependence of χ' and χ'' at an external field of 1.0 kOe for various frequency values, and of the frequency dependence of χ' and χ'' at an external field of 1.0 kOe for various temperature ranges, are given in Figures 5 and 6, respectively. The relevant Cole-Cole plots are shown in Figure 7. The frequency and temperature dependence indicate thermally assisted relaxation. From the analysis of these plots based on the generalized Debye model [38], the temperature dependence of the relaxation time in the 2.0–4.5 K temperature range was obtained. This dependence is shown in Figure 8 by plotting the quantity $\ln(\tau)$ as

a function of $1/T$. For a thermal activation process obeying the Orbach law, the plots would follow a linear relationship. Clearly this is not the case, as seen in Figure 8. Deviation from the Orbach process is often observed in 3d/4f heteronuclear complexes and has been attributed to the involvement of multiple relaxation mechanisms [39–42]. The temperature dependence of the relaxation time, τ, for **1** can be fitted with the Equation (2):

$$\frac{1}{\tau} = AT + BT^n + \left(\frac{1}{\tau_0}\right)\exp\left(-\frac{U}{k_B T}\right) \quad (2)$$

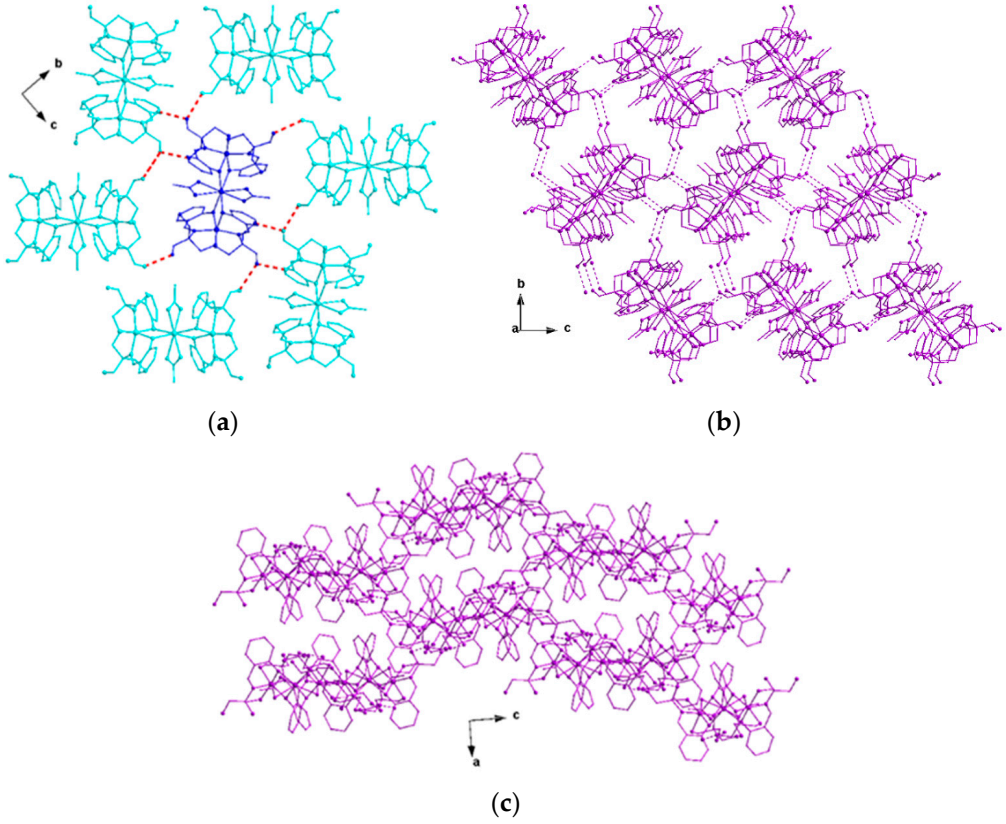

Figure 3. (**a**) The 6-connected node in **1** with hydrogen bonds shown as red dashed lines. (**b**) A small part of the 3D supramolecular network of **1** in the *bc* plane, (**c**) in the *ac* plane.

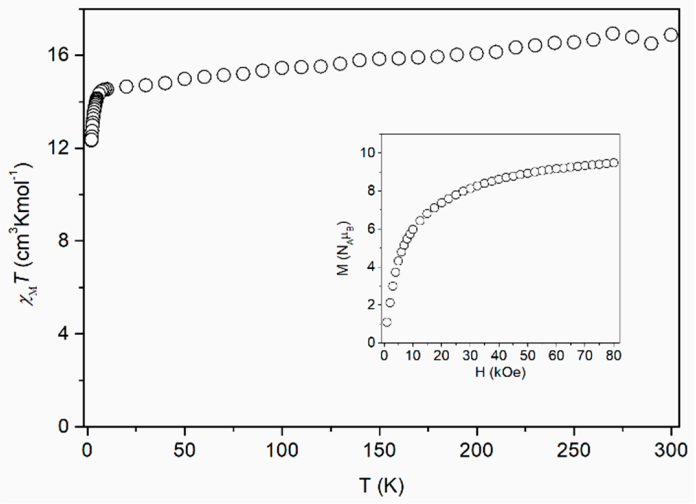

Figure 4. Plots of $\chi_M T$ vs. T at 1000 Oe and M vs. H at 2 K (inset) for **1**.

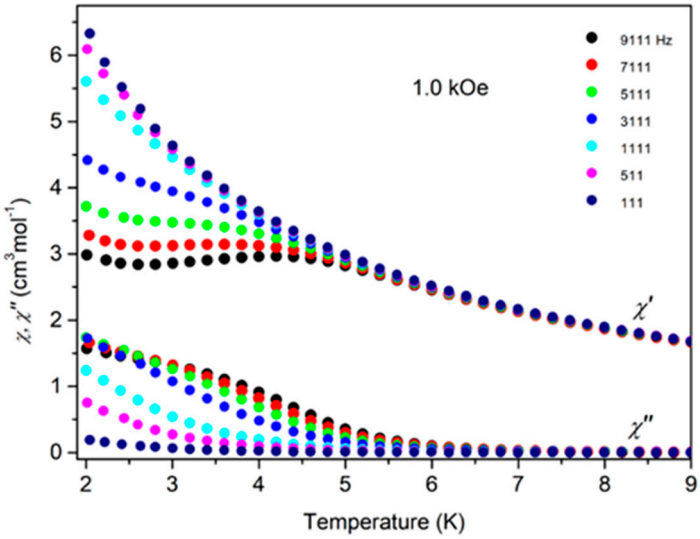

Figure 5. Plots of χ' and χ'' vs. T of **1** under various frequencies under 1.0 kOe external magnetic field.

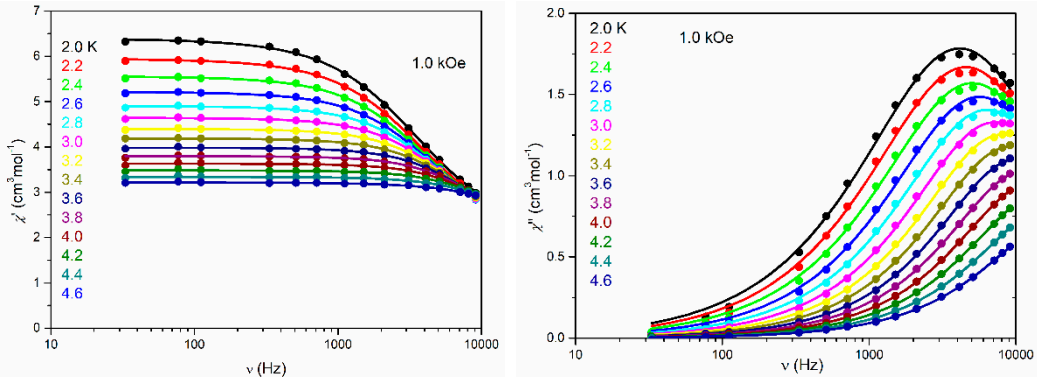

Figure 6. Plots of χ' and χ'' vs. ν of **1** at various temperatures under 1.0 kOe external magnetic field. Solid lines are fits obtained with the generalized Debye model [38].

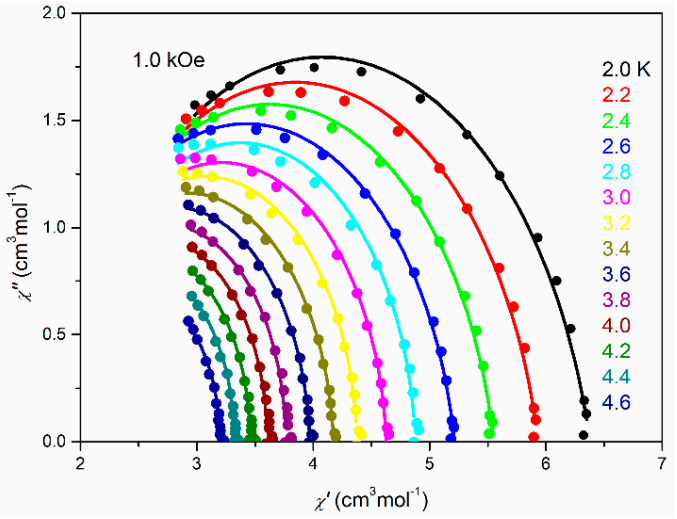

Figure 7. Cole-Cole plots for **1** at various temperatures under 1.0 kOe external magnetic field. Solid lines are fits obtained with the generalized Debye model [38].

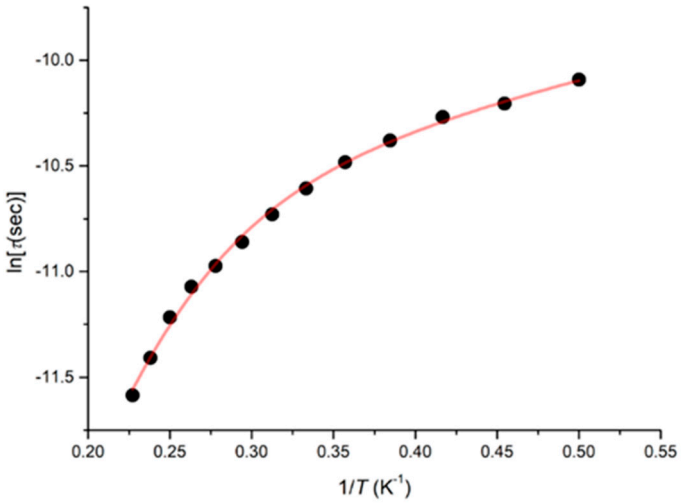

Figure 8. Plot of ln(τ) vs. $1/T$ for **1**. The red line represents the best fit according to Equation (2).

In this equation the first term in the right part of Equation (2) represents the direct process, the second term the Raman mechanism and the third the Orbach mechanism [43]. Consideration of the three mechanisms simultaneously constitutes an overparametrization. If we consider the direct and Raman mechanisms, a good fit is obtained with $A = 11.8(2) \times 10^3$ $K^{-1}s^{-1}$, $n = 6.4(3)$ and $B = 4(2)$ $K^{-6.4}s^{-1}$. For the direct and Orbach mechanisms, a good fit is obtained with $A = 13.0(2) \times 10^3$ $K^{-1}s^{-1}$, a preexponential factor $\tau_0 = 4(2) \times 10^{-8}$ s, and a thermal barrier $U = 26(2)$ K.

The temperature dependence of the magnetic susceptibility in the form of $\chi_M T$ vs. T under a magnetic field of 1 kOe is shown in Figure 9. The $\chi_M T$ product of complex **2** at 300 K is 16.29 cm^3Kmol^{-1}, which compares to the theoretical value of 16.06 cm^3Kmol^{-1}, for two non-interacting Ni^{II} ($S = 1$, $g = 2.0$) ions and one Ho^{III} ($S = 2$, $J = 8$, $g = 5/4$) ion (Figure 9). The $\chi_M T$ product of **2** decreases slightly upon decreasing of the temperature, reaching the value of 11.93 cm^3Kmol^{-1} at 20 K, and then drops rapidly to the value of 5.46 cm^3Kmol^{-1} at 2 K. The decrease of the $\chi_M T$ product at low temperatures is mainly governed by the thermal depopulation of the ground state sublevels that result from spin-orbit coupling of the Ho^{III} ion and a low symmetry crystal field. The field dependence of the magnetization for **2** is shown as inset in Figure 9. The magnetization of **2** at 2 K, reaches the value of 9.43 μ_B at 80 kOe without reaching saturation, which suggests that the ground spin state is not fully populated because other excited states remain populated to some extent even at 2 K.

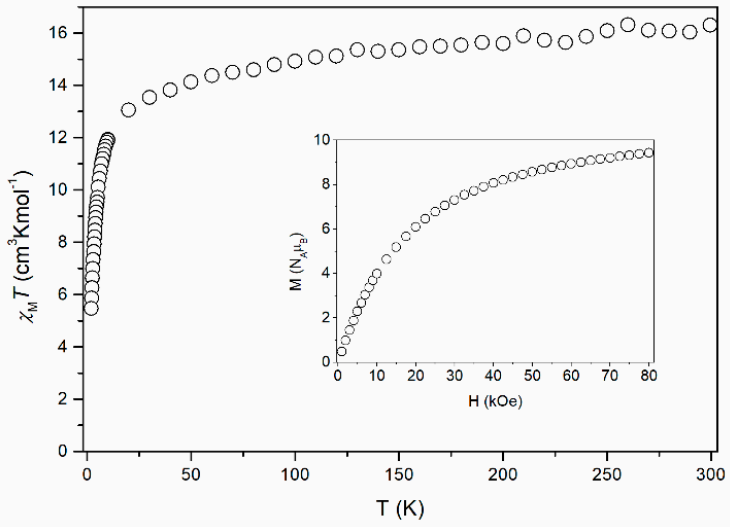

Figure 9. Plots of $\chi_M T$ vs. T at 1000 Oe and M vs. H at 2 K (inset) for **2**.

The magnetic relaxation properties of **2** was explored by AC susceptibility measurements. No slow relaxation is observed either in the absence or in the presence of an external dc magnetic field.

The temperature dependence of the magnetic susceptibility in the form of $\chi_M T$ vs. T and $1/\chi_M$ vs. T under a magnetic field of 1 kOe is shown in Figure 10. For $T > 80$ K the $1/\chi_M$ vs. T data exhibits a linear behavior that could be fitted assuming the Curie Weiss law ($1/\chi_M = (T - \theta/C)$. From the fit, a value of $C = 2.18$ cm^{3}Kmol^{-1} is determined. This value compares to two Ni^{II} ions ($S = 1$) with $g > 2.0$ and a diamagnetic Y^{III} ion. The $\chi_M T$ product remains practically constant down to ~80 K and below this temperature slowly increases reaching a broad maximum value of ~2.21 cm^{3}Kmol^{-1} at 10–15 K. This increase suggests weak intramolecular ferromagnetic interactions between the Ni^{II} ions. At lower temperatures, $\chi_M T$ decreases rapidly reaching a value of 1.58 cm^{3}Kmol^{-1} at 2 K (Figure 10). The drop of the $\chi_M T$ product at low temperatures is consistent with the single ion magnetic anisotropy (zero field splitting, zfs) of the Ni^{II} ions and/or intermolecular antiferromagnetic interactions between the molecules. Field dependent magnetization measurements at 2.2 K were performed up to 50 kOe for **3** and are shown as inset in Figure 10. The magnetization increases in low magnetic fields and reaches a final value of 3.24 μ_B for **3** at 50 kOe, without reaching saturation. The simultaneous fit of the $\chi_M T$ vs. T and M vs. H data was obtained using the spin Hamiltonian:

$$H = -2JS_{Ni1}S_{Ni2} + 2DS_{Ni}^2 \quad (3)$$

where J is the exchange coupling constant and D is the axial term of the zfs interaction. The obtained parameters, using the program PHI [44], are $J = +0.36$ cm^{-1}, $D = +5.13$ cm^{-1} with $g = 2.08$ (solid lines in Figure 10). Weak magnetic interactions between distanced Ni(II) ions have been observed also in Ni_2Ln triads [20,23] for Ln = La. In particular in the case of ref. [23] the interactions were found to be weak ferromagnetically and the parameters are very close to those observed in the present work.

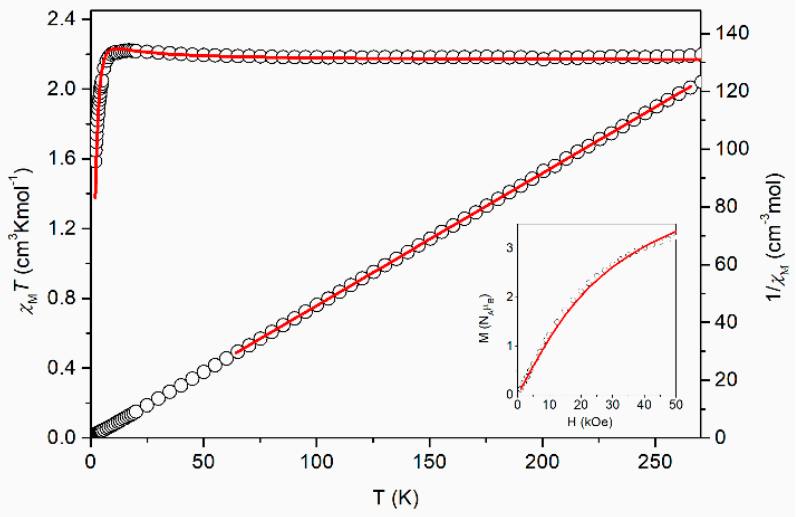

Figure 10. Plots of $\chi_M T$ vs. T and $1/\chi_M$ vs. T at 1000 Oe and M vs. H at 2.2 K (inset) for **3**. Solid lines represent the best fit obtained with the magnetic model described in the text.

As in the case of **2,** no slow relaxation is observed for **3**, either in the absence or in the presence of an external dc magnetic field.

4. Concluding Comments

We have extended the series of trinuclear complexes $[Ni_2Ln(H_3L)_4(O_2CMe)_2](NO_3)$ (Ln^{III} = Sm, Eu, Gd, Tb) previously reported [19], by using Ln^{III} = Dy, Ho and the diamagnetic ion Y^{III}. The trinuclear complexes $[Ni_2Ln(H_3L)_4(O_2CMe)_2](NO_3)$ (Ln^{III} = Dy (**1**),

Ho (**2**), Y (**3**)), which contain the monoanion of the tetradentate Schiff base ligand H_4L = *o*-C_6H_4-CH=NC$(CH_2OH)_3$, consist of almost linear trinuclear cations {Ni_2Ln} and nitrate anions. The molecular structures of **1**–**3** are isostructural to those of the complexes in [19] considering the coordination environment of the metal ions, but differ in the coordination geometry around the lanthanide ion and the pattern of intermolecular interactions. These differences may affect the crystallization of both types of complexes in different space groups, namely complexes in [19] crystallize in the centrosymmetric orthorhombic space group *P*nnn, whilst **1**–**3** crystallize in the non-centrosymmetric orthorhombic space group *P*na2_1. The latter belongs to one of the seven point groups which is synonymous to multifunctionality, as it could combine the magnetic properties with different other physical properties, which are compatible with non-centrosymmetry. It is interesting to note the fact that the studied complexes present chiral configurations without using chiral ligands, however both enantiomers coexist due to the presence of mirror plane symmetry. The magnetic study of **1** by ac susceptibility measurements revealed frequency and temperature dependent out-of-phase signals under H_{DC} = 1.0 kOe. The relaxation properties for **1** are governed by the direct and Orbach processes, or the direct and Raman processes. The magnetic behavior of **2** at low temperatures is governed by the thermal depopulation of the ground state sublevels due to the spin-orbit coupling of the Ho^{III} ion and a low symmetry crystal field. The magnetic properties of **3**, which contains the diamagnetic Y^{III} ion, revealed ferromagnetic coupling between the Ni^{II} ions and zfs effects. The absence of slow magnetic relaxation effects in **2** and **3,** as well as in the previously reported isostructural trinuclear clusters [19], suggests that the unique relaxation behavior of **1** is inherent to the Dy^{III} ion in the specific crystal field environment.

Further work is under way in an attempt to successfully isolate enantiopure crystals by following different synthetic paths or by choosing the appropriate ligands.

Supplementary Materials: The following supporting information can be downloaded at: https://www.mdpi.com/article/10.3390/cryst12010095/s1, Figure S1: Overlay diagrams of {Ni_2Tb} (red, ref. [19]) and **1** (blue, present work); Figure S2: Square antiprism polyhedron of {Ni_2Tb} (left image, ref. [19]) and biaugmented trigonal prism for **1** (right); Figure S3: (a) Packing of complexes in the structure of {Ni_2Tb} [19] and (b) in the structure of **1**; Table S1: CShM parameters for the polyhedrons around the lanthanide ion in {Ni_2Tb} and **1**–**3**.

Author Contributions: Investigation, experimental, D.D.; experimental, A.P.; methodology, measurements, magnetic data analysis, M.P. and Y.S.; methodology, measurements, crystal structure analysis, V.P. and C.P.R.; writing—original draft preparation, M.P., Y.S., V.P. and C.P.R.; writing—review and editing, M.P., Y.S., V.P. and C.P.R.; supervision, V.P. and C.P.R.; funding acquisition, D.D., V.P. and C.P.R. All authors have read and agreed to the published version of the manuscript.

Funding: This research was funded by the State Scholarships Foundation (IKY) MIS-5033021.

Institutional Review Board Statement: Not applicable.

Informed Consent Statement: Not applicable.

Data Availability Statement: The magnetic data presented in this study are available on request from the corresponding author.

Acknowledgments: This research is co-financed by Greece and the European Union (European Social Fund—ESF) through the Operational Programme "Human Resources Development, Education and Lifelong Learning" in the context of the project "Reinforcement of Postdoctoral Researchers—2nd Cycle" (MIS-5033021), implemented by the State Scholarships Foundation (IKϒ). V.P. would like to thank the Special Account of NCSR "Demokritos" for financial support regarding the operation of the X-ray facilities at INN through the internal program entitled 'Structural study and characterization of crystalline materials' (NCSR Demokritos, ELKE #10 813).

Conflicts of Interest: The authors declare no conflict of interest.

Appendix A

CCDC 2128930–2128932 contain the supplementary crystallographic data for this paper. These data can be obtained free of charge from The Cambridge Crystallographic Data Centre via www.ccdc.cam.ac.uk/data_request/cif (accessed on 1 December 2021). Overlay diagrams of complex {Ni_2Tb} reported in [19] and complex **1** showing the structural similarity of both cationic complexes which crystallize in different space groups (Figure S1). Figures of the different coordination polyhedral around the lanthanide ion in complexes {Ni_2Tb} [19] and **1** (Figure S2). Figure showing the different patterns of intermolecular packing structures between complexes {Ni_2Tb} [19] and **1** (Figure S3). Table listing the CShM parameters for the polyhedrons around the lanthanide ions in {Ni_2Tb} [19] and **1–3** (Table S1).

References

1. Vopson, M.M. Fundamentals of Multiferroic Materials and Their Possible Applications. *Crit. Rev. Solid State Mater. Sci.* **2015**, *40*, 223–250. [CrossRef]
2. Train, C.; Gruselle, M.; Verdaguer, M. The fruitful introduction of chirality and control of absolute configurations in molecular magnets. *Chem. Soc. Rev.* **2011**, *40*, 3297–3312. [CrossRef]
3. Cosquer, G.; Shen, Y.; Almeida, M.; Yamashita, M. Conducting single-molecule magnet materials. *Dalton Trans.* **2018**, *47*, 7616–7627. [CrossRef] [PubMed]
4. Bhatt, P.; Mukadam, M.D.; Meena, S.S.; Mishra, S.K.; Mittal, R.; Sastry, P.U.; Mandal, B.P.; Yusuf, S.M. Room temperature ferroelectricity in one-dimensional single chain molecular magnets [{M(Δ)M(Λ)}$(ox)_2(phen)_2]_n$ (*M* = Fe and Mn). *Appl. Phys. Let.* **2017**, *110*, 102901. [CrossRef]
5. Guo, P.H.; Liu, J.L.; Jia, J.H.; Wang, J.; Guo, F.-S.; Chen, Y.-C.; Lin, W.-Q.; Leng, J.-D.; Bao, D.-H.; Zhang, X.-D.; et al. Multifunctional Dy^{III}_4 cluster exhibiting white-emitting, ferroelectric and single-molecule magnet behavior. *Chem. Eur. J.* **2013**, *19*, 8769–8773. [CrossRef]
6. Jia, J.-H.; Li, Q.-W.; Chen, Y.-C.; Liu, J.-L.; Tong, M.-L. Luminescent single-molecule magnets based on lanthanides: Design strategies, recent advances and magneto-luminescent studies. *Coord. Chem. Rev.* **2019**, *378*, 365–381. [CrossRef]
7. Inglis, R.; White, F.; Piligkos, P.; Wernsdorfer, W.; Brechin, E.K.; Papaefstathiou, G.S. Chiral single-molecule magnets: A partial Mn(III) supertetrahedron from achiral components. *Chem. Commun.* **2011**, *47*, 3090–3092. [CrossRef] [PubMed]
8. Mazarakioti, E.C.; Poole, K.M.; Cunha-Silva, L.; Christou, G.; Stamatatos, T.C. A new family of Ln_7 clusters with an ideal D_{3h} metal-centered trigonal prismatic geometry, and SMM and photoluminescence behaviors. *Dalton Trans.* **2014**, *43*, 11456–11460. [CrossRef] [PubMed]
9. Zaleski, C.M.; Depperman, E.C.; Kampf, J.W.; Kirk, M.L.; Pecoraro, V.L. Synthesis, structure, and magnetic properties of a large lanthanide-transition-metal single-molecule magnet. *Angew. Chem. Int. Ed. Engl.* **2004**, *43*, 3912–3914. [CrossRef] [PubMed]
10. Zhao, L.; Wu, J.; Xue, S.; Tang, J. A linear 3d-4f tetranuclear $Co^{III}_2Dy^{III}_2$ single-molecule magnet: Synthesis, structure, and magnetic properties. *Chem. Asian J.* **2012**, *7*, 2419–2423. [CrossRef]
11. Peng, Y.; Kaemmerer, H.; Powell, A.K. From the {$Fe^{III}_2Ln_2$} butterfly's perspective: The magnetic benefits and challenges of cooperativity within 3d-4f based coordination clusters. *Chem. Eur. J.* **2021**, *27*, 15043–15065. [CrossRef]
12. Peng, J.-B.; Zhang, Q.-C.; Kong, X.-J.; Ren, Y.-P.; Long, L.-S.; Huang, R.-B.; Zheng, L.-S.; Zheng, Z. A 48-metal cluster exhibiting a large magnetocaloric effect. *Angew. Chem. Int. Ed. Engl.* **2011**, *45*, 10837–10840. [CrossRef]
13. Song, X.-Q.; Liu, P.-P.; Wang, C.-Y.; Liu, Y.-A.; Liu, W.-S.; Zhang, M. Three sandwich-type zinc(ii)-lanthanide(iii) clusters: Structures, luminescence and magnetic properties. *RSC Adv.* **2017**, *7*, 22692–22698. [CrossRef]
14. Li, Q.; Qian, J.; Tian, C.; Lin, P.; He, Z.; Wang, N.; Shen, J.; Zhang, H.; Chu, T.; Yuan, D.; et al. Butterfly-like enantiomerically homochiral {$Co^{II}_6Co^{III}_4$} clusters exhibiting both slow magnetic relaxation and ferroelectric property. *Dalton Trans.* **2014**, *43*, 3238–3243. [CrossRef] [PubMed]
15. Long, J.; Rouquette, J.; Thibaud, J.-M.; Ferreira, R.A.S.; Carlos, L.D.; Donnadieu, B.; Vieru, V.; Chibotaru, L.F.; Konczewicz, L.; Haines, J.; et al. A high-temperature molecular ferroelectric Zn/Dy complex exhibiting single-ion-magnet behavior and lanthanide luminescence. *Angew. Chem. Int. Ed. Engl.* **2015**, *54*, 2236–2240. [CrossRef]
16. Chandrasekhar, V.; Pandian, B.M.; Azhakar, R.; Vittal, J.J.; Clérac, R. Linear trinuclear mixed-metal Co^{II}-Gd^{III}-Co^{II} single-molecule magnet: $[L_2Co_2Gd][NO_3]\cdot 2CHCl_3$ (LH_3 =(S)P[N(Me)N=CH-C_6H_3-2-OH-3-OMe]$_3$). *Inorg. Chem.* **2007**, *46*, 5140–5142. [CrossRef] [PubMed]
17. Jesudas, J.J.; Pham, C.T.; Hagenbach, A.; Abram, U.; Nguyen, H.H. Trinuclear $Co^{II}Ln^{III}Co^{II}$ complexes (Ln = La, Ce, Nd, Sm, Gd, Dy, Er, and Yb) with 2,6-dipicolinoylbis(*N*,*N*-diethylthiourea): Synthesis, structures, and magnetism. *Inorg. Chem.* **2020**, *59*, 386–395. [CrossRef]
18. Raptopoulou, C.P. Heterometallic complexes containing the Ni^{II}-Ln^{III}-Ni^{II} moiety- structures and magnetic properties. *Crystals* **2020**, *10*, 1117. [CrossRef]
19. Georgopoulou, A.N.; Pissas, M.; Psycharis, V.; Sanakis, Y.; Raptopoulou, C.P. Trinuclear Ni^{II}-Ln^{III}-Ni^{II} complexes with Schiff base ligands: Synthesis, structure, and magnetic rroperties. *Molecules* **2020**, *25*, 2280. [CrossRef]

20. Chandrasekhar, V.; Pandian, B.M.; Boomishankar, R.; Steiner, A.; Vittal, J.J.; Houri, A.; Clérac, R. Trinuclear heterobimetallic Ni_2Ln complexes $[L_2Ni_2Ln][ClO_4]$ (Ln = La, Ce, Pr, Nd, Sm, Eu, Gd, Tb, Dy, Ho, and Er; LH_3 = (S)P[N(Me)N=CH-C_6H_3-2-OH-3-OMe]$_3$): From simple paramagnetic complexes to single-molecule magnet behavior. *Inorg. Chem.* **2008**, *47*, 4918–4929. [CrossRef] [PubMed]
21. Yao, M.-X.; Zhu, Z.-X.; Lu, X.-Y.; Deng, X.-W.; Jing, S. Rare single-molecule magnets with six-coordinate Ln^{III} ions exhibiting a trigonal antiprism configuration. *Dalton Trans.* **2016**, *45*, 10689–10695. [CrossRef] [PubMed]
22. Wen, H.-R.; Zhang, J.-L.; Liang, F.-Y.; Yang, K.; Liu, S.-J.; Liao, J.-S.; Liu, C.-M. Tb^{III}/3d-Tb^{III} clusters derived from a 1,4,7-triazacyclononane-based hexadentate ligand with field-induced slow magnetic relaxation and oxygen-sensitive luminescence. *New J. Chem.* **2019**, *43*, 4067–4074. [CrossRef]
23. Upadhyay, A.; Das, C.; Langley, S.K.; Murray, K.S.; Srivastava, A.K.; Shanmugam, M. Heteronuclear Ni(II)-Ln(III) (Ln = La, Pr, Tb, Dy) complexes: Synthesis and single-molecule magnet behaviour. *Dalton Trans.* **2016**, *45*, 3616–3626. [CrossRef] [PubMed]
24. Upadhyay, A.; Komatireddy, N.; Ghirri, A.; Tuna, F.; Langley, S.K.; Srivastava, A.K.; Sañudo, E.C.; Moubaraki, B.; Murray, K.S.; McInnes, E.J.L.; et al. Synthesis and magnetothermal properties of a ferromagnetically coupled Ni^{II}-Gd^{III}-Ni^{II} cluster. *Dalton Trans.* **2014**, *43*, 259–266. [CrossRef] [PubMed]
25. Costes, J.-P.; Yamaguchi, T.; Kojima, M.; Vendier, L. Experimental evidence for the participation of 5d Gd^{III} orbitals in the magnetic interaction in Ni-Gd complexes. *Inorg. Chem.* **2009**, *48*, 5555–5561. [CrossRef]
26. Comba, P.; Enders, M.; Großhauser, M.; Hiller, M.; Müller, D.; Wadepohl, H. Solution and solid state structures and magnetism of a series of linear trinuclear compounds with a hexacoordinate Ln^{III} and two terminal Ni^{II} centers. *Dalton Trans.* **2017**, *46*, 138–149. [CrossRef] [PubMed]
27. Raptopoulou, C.P.; Sanakis, Y.; Psycharis, V.; Pissas, M. Zig-zag [Mn^{III}_4] clusters from polydentate Schiff base ligands. *Polyhedron* **2013**, *64*, 181–188. [CrossRef]
28. Rigaku/MSC. *CrystalClear*; Rigaku/MSC Inc.: The Woodlands, TX, USA, 2005.
29. Sheldrick, G.M. A short history of SHELX. *Acta Cryst.* **2008**, *A64*, 112–122.
30. Sheldrick, G.M. Crystal structure refinement with SHELXL. *Acta Cryst.* **2015**, *C71*, 3–8.
31. Impact, C. DIAMOND—Crystal and Molecular Structure Visualization. Ver. 3.1. *Cryst. Impact* **2014**.
32. Mounika, K.; Anupama, B.; Pragathi, J.; Gyanakumari, C. Synthesis, characterization and biological activity of a Schiff base derived from 3-ethoxy salicylaldehyde and 2-amino benzoic acid and its transition metal complexes. *J. Sci. Res.* **2010**, *2*, 513–524. [CrossRef]
33. Deacon, G.B.; Phillips, R.J. Relationships between the carbon-oxygen stretching frequencies of carboxylato complexes and the type of carboxylate coordination. *Coord. Chem. Rev.* **1980**, *33*, 227–250. [CrossRef]
34. Patil, K.C.; Chandrashekhar, G.V.; George, M.V.; Rao, C.N.R. Infrared spectra and thermal decompositions of metal acetates and dicarboxylates. *Can. J. Chem.* **1968**, *46*, 257–265. [CrossRef]
35. Ribot, F.; Toledano, P.; Sanchez, C. X-Ray and spectroscopic investigations of the structure of yttrium acetate tetrahydrate. *Inorg. Chim. Acta* **1991**, *185*, 239–245. [CrossRef]
36. Nakamoto, K. *Infrared and Raman Spectra of Inorganic and Coordination Compounds*, 4th ed.; Wiley: New York, NY, USA, 1986.
37. Llunell, M.; Casanova, D.; Girera, J.; Alemany, P.; Alvarez, S. *SHAPE*, version 2.0; Universitat de Barcelona: Barcelona, Spain, 2010.
38. Pissas, M.; Psycharis, V.; Raptopoulou, C.; Sanakis, Y. *Unique Magnetic Properties in Single-Molecule Magnets: Molecular Architectures and Building Blocks for Spintronics*; Wiley-VCH Verlag GmbH & Co.: Weinheim, Germany, 2019.
39. Car, P.-E.; Favre, A.; Caneschi, A.; Sessoli, R. Single molecule magnet behaviour in a rare trinuclear {$Cr^{III}Dy^{III}_2$} methoxo-bridged complex. *Dalton Trans.* **2015**, *44*, 15769–15773. [CrossRef] [PubMed]
40. Then, P.L.; Takehara, C.; Kataoka, Y.; Nakano, M.; Yamamura, T.; Kaziwara, T. Structural switching from paramagnetic to single-molecule magnet behaviour of $LnZn_2$ trinuclear complexes. *Dalton Trans.* **2015**, *44*, 18038–18048. [CrossRef] [PubMed]
41. Mayans, J.; Saetz, Q.; Font-Bardia, M.; Escuer, A. Enhancement of magnetic relaxation properties with 3d diamagnetic cations in [$Zn^{II}Ln^{III}$] and [$Ni^{II}Ln^{III}$], Ln^{III} = Kramers lanthanides. *Dalton Trans.* **2019**, *48*, 641–652. [CrossRef]
42. Xi, L.; Sun, J.; Wang, K.; Lu, J.; Jing, P.; Li, L. Slow magnetic relaxation in Co^{II}-Ln^{III} heterodinuclear complexes achieved through a functionalized nitronyl nitroxide biradical. *Dalton Trans.* **2020**, *49*, 1089–1096. [CrossRef]
43. Abragam, A.; Bleaney, B. *Electron Paramagnetic Resonance of Transition Ions*; Dover Publ.: New York, NY, USA, 1986.
44. Chilton, N.F.; Anderson, R.P.; Turner, L.D.; Soncini, A.; Murray, K.S. PHI: A powerful new program for the analysis of anisotropic monomeric and exchange-coupled polynuclear d- and f-block complexes. *J. Comput. Chem.* **2013**, *34*, 1164–1175. [CrossRef]